CHALMERS

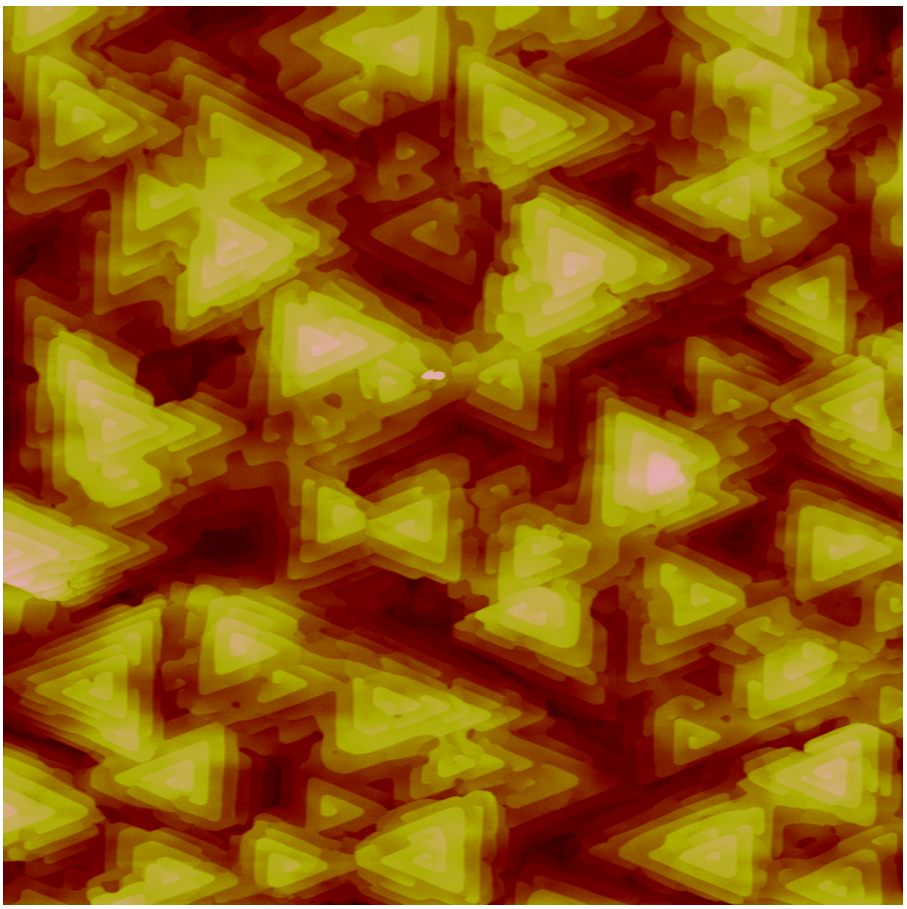

Characterization of Bismuth Telluride Thin Films Grown by MBE

Master's thesis in Wireless, Photonics and Space Engineering

ATTILA FÜLÖP

Department of Microtechnology and Nanoscience - MC2
Photonics Laboratory
CHALMERS UNIVERSITY OF TECHNOLOGY
Göteborg, Sweden 2013

MASTER'S THESIS IN WIRELESS, PHOTONICS AND SPACE ENGINEERING

Characterization of Bismuth Telluride Thin Films Grown by MBE

ATTILA FÜLÖP

Department of Microtechnology and Nanoscience - MC2

Photonics Laboratory

CHALMERS UNIVERSITY OF TECHNOLOGY

Göteborg, Sweden 2013

Characterization of Bismuth Telluride Thin Films Grown by MBE
ATTILA FÜLÖP

Master's thesis
Department of Microtechnology and Nanoscience - MC2
Photonics Laboratory
Chalmers University of Technology
SE-412 96 Göteborg
Sweden
Telephone: +46 (0)31-772 1000

Cover:
AFM scan showing bismuth telluride spiral island growth.

Chalmers Reproservice
Göteborg, Sweden 2013

Characterization of Bismuth Telluride Thin Films Grown by MBE
Master's thesis in Wireless, Photonics and Space Engineering
ATTILA FÜLÖP
Department of Microtechnology and Nanoscience - MC2
Photonics Laboratory
Chalmers University of Technology

Abstract

Bismuth telluride, Bi_2Te_3, has been predicted to be a topological insulator; it has however been difficult to manufacture good quality thin films of it. This project focuses on the characterization and analysis of bismuth telluride thin films that have been manufactured using molecular beam epitaxy in the Chalmers cleanroom. Substrate material and several growth condition parameters have been varied and are here analyzed using X-ray diffraction and atomic force microscopy to draw conclusions about the optimal growth conditions. It turns out that the growth mode of the bismuth telluride thin films changes when grown on vicinal vs. flat substrates. Other effects include a phase change from Bi_2Te_3 to Bi_4Te_3 when the tellurium flux is decreased below 20 times the bismuth flux. This phase change leads to the destruction of the topological insulator properties.

Keywords: Bismuth telluride, Bi_2Te_3, Bi_4Te_3, Topological insulator, Atomic force microscopy, AFM, X-ray diffraction, XRD, Molecular beam epitaxy, MBE

Acknowledgements

I want to start by giving my most sincere thanks to my supervisor Yuxin Song (宋禹忻) who has helped and guided me along this project. His patience and willingness to explain, answer and discuss any questions I have had really helped me learn a lot.

I would also like to thank my examiner, Shumin Wang, for giving me this opportunity and for all the discussions we have had during this time.

Last but not least, I would like to thank all the members of the Photonics Lab, including my master's student colleagues, for the discussions and the pleasant community in general.

Contents

List of publications

Paper I Attila Fülöp, Yuxin Song, Sophie Charpentier, Peixiong Shi, Maria Ekström, Luca Galletti, Floriana Lombardi and Shumin Wang, *"Phase transition of bismuth telluride thin films grown by MBE"*, Under preparation.

Paper II Yuxin Song, Sophie Charpentier, Attila Fülöp, Maria Ekström, Luca Galletti, Floriana Lombardi, Shumin Wang, *"Growth mechanism study of bismuth telluride thin films with superior transport properties for topological insulators"*, Under preparation.

Chapter 1

Introduction

New materials for semiconductor devices are continuously investigated and discovered. Among the group V elements bismuth is one of the historically least researched ones. It is the heaviest non-radioactive element and has during the past few years been found to have some interesting properties. This project will focus on the compound bismuth telluride, Bi_2Te_3, a crystal with properties that make it interesting for several different applications.

1.1 Bismuth telluride

Bismuth telluride has historically been used for thermoelectric applications because of its high figure of merit, ZT[1]. Recently however, it has been shown to have more exotic physical properties. When manufactured cleanly enough it has been predicted[2] and demonstrated[3, 4] to be a topological insulator, a material that is insulating in its bulk and conducting on its surface.

Bi_2Te_3 has a layered crystal structure, not totally unlike that of graphene. It belongs to the trigonal space group $R\bar{3}m$ but is usually described to have a hexagonal structure with a large unit cell. The hexagonal unit cell is 30 Å tall and contains three quintuple layers of Te-Bi-Te-Bi-Te. Each quintuple layer is only weakly bonded to the next with van der Waals bonds. A schematic of the unit cell can be seen in Figure (1.1)[5].

1.2 Thermoelectric effect

A thermoelectric device consists of a junction between two conducting materials. One of them contains excess holes, while the other contains excess electrons. By applying current in one direction the carriers separate and effectively cool the junction, while by applying heat to the junction a current is generated in the opposite direction[1].

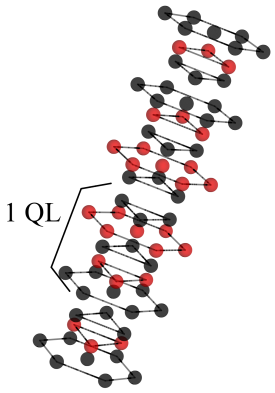

Figure (1.1): The layered structure of a Bi_2Te_3 unit cell. Black rings correspond to tellurium atoms while the red ones are bismuth atoms. One Te-Bi-Te-Bi-Te quintuple layer is marked.

The cooling effect discovered by Jean Peltier in 1834 can be described by Equation (1.1):

$$\frac{dQ}{dt} = \Pi I, \tag{1.1}$$

where I is the current driven through the junction and Π is the Peltier coefficient of the junction that depends on the two materials according to $\Pi = (S_\mathrm{p} - S_\mathrm{n})T$. The Seebeck coefficients, S_p and S_n, are properties of each material that describe the voltage between the two ends of the given material when placed in a temperature gradient. The temperature T is the temperature of the junction.

To be able to compare different thermoelectric devices, the *figure of merit*, ZT, can be used as defined in Equation (1.2):

$$ZT = \frac{(S_\mathrm{p} - S_\mathrm{n})^2}{\rho\kappa}T. \tag{1.2}$$

Here ρ and κ describe the electrical resistivity and thermal conductivity of the device. A ZT value of 1 corresponds to roughly 10 % Carnot efficiency, while a ZT of ∞ would correspond to 100 %[1].

1.3 Topological insulators

The term topological insulator describes a material that is insulating in its bulk and conducting on its surface[6, 7].

Many properties of a material can be described by, or derived from, its electronic states and bands. The simplest topologically ordered state, the quantum Hall state, occurs when

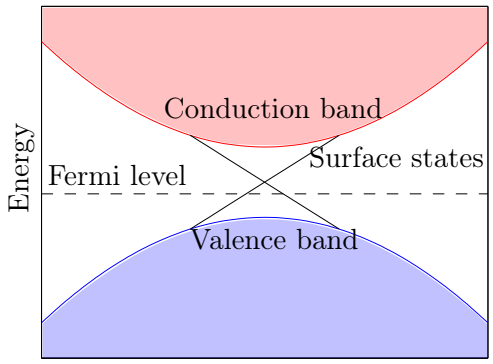

Figure (1.2): Simplified topological insulator band structure.

a strong magnetic field is applied to a 2D electron gas between two semiconductors[8, 9]. Due to the resulting Lorentz force the electrons will enter quantized orbits within the material. However, at the edges, these orbits will bounce and lead to an electronic state that conducts in one direction[10].

A 2D topological insulator however, does not require an applied magnetic field to conduct at the edges. The inherent spin-orbit coupling is enough to cause similar effects in heavier nuclei. This leads to conductance in both directions, where the direction depends on the spin of the electron due to the spin-dependence of the spin-orbit coupling. A 3D topological insulator behaves in a similar way, here the direction of the conductance also depends on the spin of the electron, however it does so in a continuous manner[10–12].

A simplified band structure for a topological insulator can be seen in Figure (1.2). In the bulk, there is the visible band gap between the conduction and the valence band. As long as the Fermi level stays within the band gap, we have insulating behaviour. The position of the Fermi level is of course dependent on doping and defect densities. On the material surface however, there are states that connect the two bands and lead to conductivity.

Chapter 2

Experiment and tools

The Bi_2Te_3 samples were grown using molecular beam epitaxy (MBE) and were measured and characterized by X-ray diffraction (XRD), atomic force microscopy (AFM) and Hall measurements. This chapter will describe the working principles of these techniques.

2.1 Molecular beam epitaxy

Molecular beam epitaxy is one way to grow, or deposit, crystalline materials. This fabrication method allows materials to grow atomic layer by atomic layer[13].

2.1.1 MBE basics

The general principle is that a substrate is placed upside-down in a growth chamber that is kept in ultra-high vacuum. Several different material sources are attached to the bottom of this chamber. Each material source can be controlled and streamed onto the substrate separately or together. To deposit a material, it has to be heated up and a shutter has to be opened between it and the substrate. This gives a very slow and precisely controllable environment for thin film and crystal growth.

By adjusting the substrate temperature and the source temperatures it is possible to fine-tune the growth conditions to match the intended speed and relative material concentrations.

2.1.2 Choice of substrate

In general, greater lattice constant mismatch leads to more defects and thus worse crystal quality. However, for Bi_2Te_3, we have van der Waals bonds between the quintuple layers

which means that it should be able to relax and avoid strain very quickly[14] and thus have less strict requirements on lattice matching.

The available substrates are Si(111), GaAs(100), GaAs(111), GaN and GaSb. Out of these Si(111) and GaAs(111) have a fitting crystal structure with 14 % and 9.5 % lattice mismatches respectively.

A vicinal substrate is a substrate where the surface has been cut at a small angle, so that the primary crystal direction is no longer pointing perpendicularly out of the surface. It has been noted that Bi_2Se_3, a crystal very similar to Bi_2Te_3 in terms of structure, has better growth characteristics when grown on vicinal Si substrates compared to flat ones[15, 16]. This is due to the fact that vicinal substrates suppress crystal twinning and screw dislocations[17, 18]. The same kind of effect has also been seen with Bi_2Te_3[19]. Here however the step-flow growth mode on the vicinal substrates does not necessarily give better crystal characteristics than the spiral growth on the flat substrates.

2.1.3 Substrate preparation

Before growth of Bi_2Te_3 can start, the native oxide layer that has been formed on the top of the substrate has to be removed. This is typically done inside the MBE machine by heating. After the oxide layer has been removed the ideal substrate would be completely flat. To compensate for any substrate surface roughness it is possible to grow a few layers of the substrate material before the bismuth telluride. This may not always be trivial, if the preferred growth direction of the substrate crystal is different than the z direction of the substrate.

2.2 X-ray diffraction

By using X-ray diffraction it is possible to determine and analyze the crystal structure of a material. The method is based on Bragg's law and is realized using commercially available equipment together with MATLAB scripts for the analysis.

2.2.1 Bragg's law

Bragg's law states that if an incident beam reflects on two different planes that are just the right distance apart, the reflected beam will show constructive interference according to Equation (2.1):

$$2d \sin\theta = n\lambda. \tag{2.1}$$

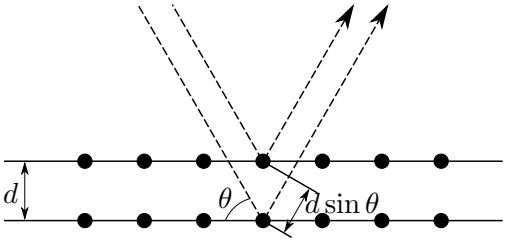

Figure (2.1): Concept of Bragg diffraction. Based on "Bragg diffraction planes"[20].

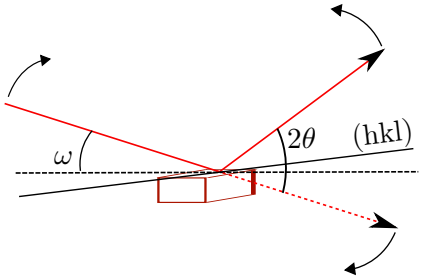

Figure (2.2): Concept of an ω-2θ scan. Based on "X-ray diffraction transmission"[21].

Here d is the distance between the planes that cause the diffraction, n is the order, λ is the wavelength of the X-rays and θ is the incident angle (compared to the crystal plane, not the sample surface!), see Figure (2.1) for an illustration. Using this model, it is possible to draw conclusions about the structure of the crystal by shining light on it from different angles.

2.2.2 Equipment

A Philips X'Pert Materials Research Diffractometer (MRD) was used to do the XRD measurements. It contains a goniometer which allows the sample to be rotated along all axes. The radiation comes from a CuKα source combined with a Ge[220] 4-crystal monochromator that in the end provides X-rays with wavelength $\lambda_{\mathrm{CuK}\alpha 1} = 1.5406\,\text{Å}$.

2.2.3 ω-2θ scans

The scan method used for the XRD measurements is called an ω-2θ scan. The angle ω is the angle between the sample surface and the incident beam. It is important to note that this is not the same thing as θ, which is the angle between the crystal plane and the incident (and diffracted) beam, see Figure (2.2) for an illustration.

Before an ω-2θ scan is done, the measurement setup first has to be calibrated to a known peak. This is usually a peak that belongs to the substrate. By optimizing all

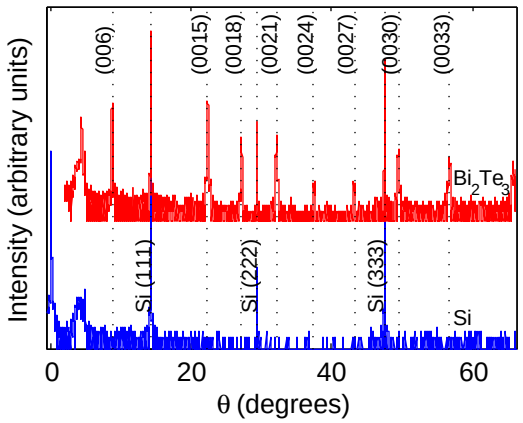

Figure (2.3): Example of an ω-2θ scan containing Si and Bi_2Te_3 peaks. The bottom blue rocking curve is the result of an ω-2θ scan of a pure Si substrate while the upper red curve is an ω-2θ scan of a Bi_2Te_3 sample on a Si substrate. Note that the Si peaks are present in both curves.

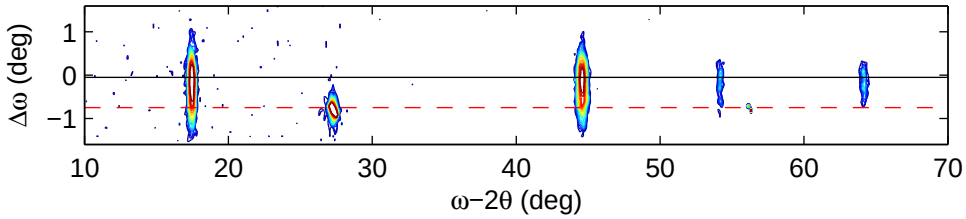

Figure (2.4): Example of a mapping scan showing misaligned peaks. The black solid line shows the center of the Bi_2Te_3 peaks while the red dotted line goes through the center of the Si substrate peaks. Here the Bi_2Te_3 layer is misaligned by 0.7° compared to the Si(111) substrate as can be seen on the y axis.

available angles, usually called ω, φ and ψ, this peak is made as narrow and as tall as possible. The variables φ and ψ describe the sample's in-plane rotation and the sample's tilt perpendicular to ω.

The ω-2θ scan itself is done by sweeping ω and 2θ together to get a plot, a rocking curve, that can identify all the planes parallel to the chosen first reference peak. This can be used to, at least partially, identify and characterize the crystalline material grown on top of the substrate. An example of a curve from an ω-2θ scan can be seen in Figure (2.3).

2.2.4 Mapping scans

While using ω-2θ scans is good for basic identification of crystal planes in one direction, it doesn't tell us anything about the alignment of the planes. If, let's say, the Bi_2Te_3

$(00l)$ planes are not perfectly aligned with the Si(111) plane of the substrate, an ω-2θ scan might only show a very weak peak or even miss them completely. This is where the 2D mapping scans come in. On the x axis, these scans vary ω together with θ just like before, but on the y axis ω is varied alone, which results in a map where one can spot and identify peaks that are slightly misaligned compared to their expected positions. An example of this can be seen in Figure (2.4).

2.3 Atomic force microscopy

When analyzing samples grown with molecular beam epitaxy, regular optical microscopy can not be used. This is due to the fact that the wavelength of visible light is more than a hundred times longer than the differences in height that we are interested in measuring. Instead, a technique called *atomic force microscopy* is used.

2.3.1 Basics

In general, AFM is a measurement where a very sharp tip attached to a cantilever is used to scan the surface of a sample. This is done by shining a laser on the tip and measuring the reflection using a position sensitive photodetector. The tip is kept at a constant height compared to the sample surface using a piezoelectric motor and feedback from the detector, see Figure (2.5) for a basic block diagram. There are several different ways that can be used to scan the surface of a sample. The mode used in this project is called the tapping mode.

2.3.2 Tapping mode

The term *tapping mode* describes a mode of operation where the tip is oscillating near its resonance frequency. When the tip gets close to the sample surface the oscillation amplitude decreases due to van der Waals forces. The tip is kept at a constant distance from the surface by keeping this amplitude constant. This mode causes less damage to both the tip and the sample than the *contact mode*, where the deflection of a stationary tip is measured, while only slightly decreasing the resolution.

2.3.3 Measuring step heights

Measuring steps by plotting the height as a function of position along a line on the sample is very sensitive to noise and will not lead to clear enough steps to be able to give an accurate value for the step height. This is solved by giving this line on the sample a width over which the heights are averaged. If the line is then drawn perpendicularly to the step,

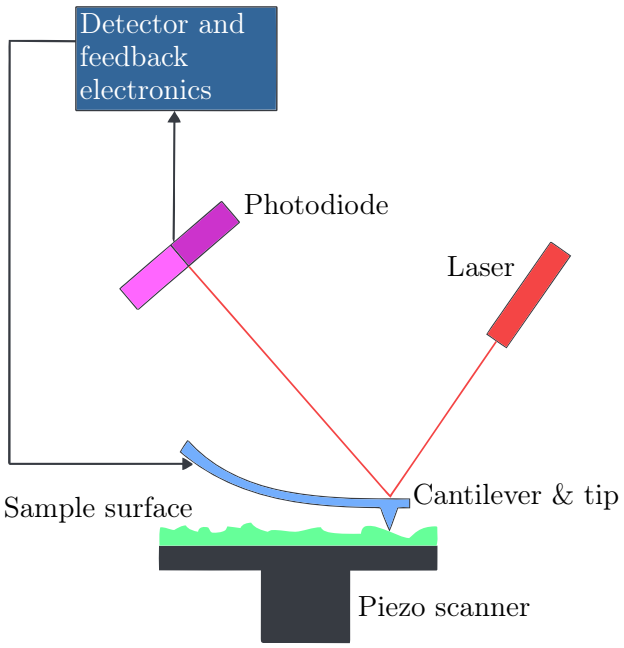

Figure (2.5): Block diagram showing the basic components of an AFM setup. Based on "Atomic force microscope block diagram"[22].

this will lead to a clear measurable step, see Figure (2.6) for an example showing the difference.

2.3.4 Sources of error

The AFM scans are sensitive to both the tip condition and the sample's surface. This can lead to some uncertainty regarding the resolution of the scans as well as the accuracy of the visible details.

If the tip is worn or dirty, the resolution of the scans, both in horizontal and vertical directions, will be reduced. This will also cause artifacts, or extra non-existent details, to appear in the images.

After a scan is done, some extra post processing is necessary for the step height measurements to be correct. Surfaces that are flat in reality might appear tilted in the scans due to the way the internal height averaging works, this needs to be corrected for. Only after the flat areas have been made flat can the step height measurements be performed. Depending on how noisy the scan is, this flattening can be more or less accurate and thus cause some uncertainty in the step height measurements.

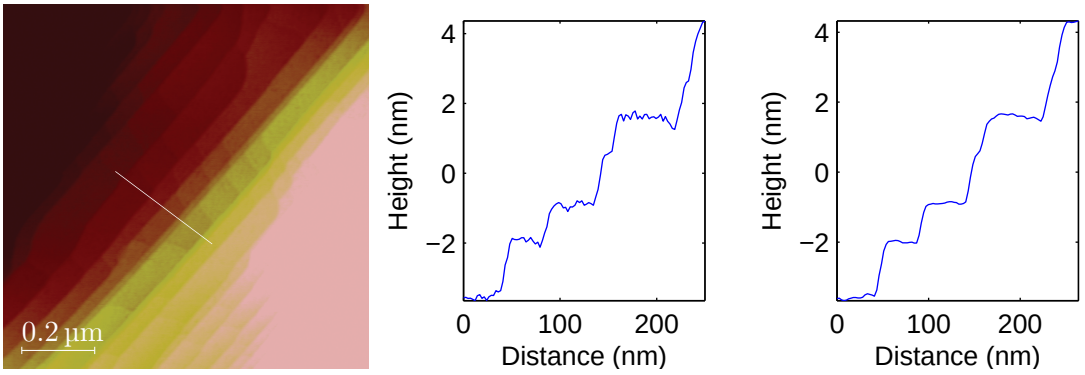

(a) AFM scan of a region with steps. The white line is where the step scans were made.

(b) Height as a function of location along the line.

(c) Height as a function of location along the line with a 40 nm wide averaging.

Figure (2.6): Height curves showing the steps on the surface of a sample illustrating the advantage of width averaging.

2.4 Hall measurements

Since Bi_2Te_3 is supposed to be a topological insulator, the electric transport properties of the manufactured thin films are of interest. Hall measurements are used to measure the carrier density and mobility in a material. This can be used to get a picture of the amount of impurities and scattering centers in the Bi_2Te_3 thin film.

2.4.1 The Lorentz force

The Hall effect is exploiting the effects of the Lorentz force, which basically states that a moving charged particle in a perpendicular magnetic field feels a force perpendicular to both the velocity of the particle and the magnetic field. The exact formulation can be seen in Equation (2.2):

$$\boldsymbol{F} = q(\boldsymbol{E} + (\boldsymbol{v} \times \boldsymbol{B})). \tag{2.2}$$

2.4.2 The Hall bar

The Lorentz force results in a potential difference between the two ends of the material according to Equation (2.3):

$$U_{\mathrm{H}} = R_{\mathrm{H}} B I \tag{2.3}$$

where U_{H} is the Hall voltage, B the magnetic field, I the current and R_{H} is the Hall coefficient according to $R_{\mathrm{H}} = -1/(n|e|d)$ with n being the electron density, $|e|$ being the elementary charge and d the thickness of the material[23].

By connecting probes to four corners of the sample it is possible to send current and measure in all interesting directions. This will in the end give us the surface carrier density, n_{s}, and the mobility, μ, shown in equations (2.4) and (2.5)[23]:

$$n_{\mathrm{s}} = \frac{1}{|e|\mathrm{d}\rho_{xy}/\mathrm{d}B}\Big|_{B=0,} \tag{2.4}$$

$$\mu = \frac{\mathrm{d}\rho_{xy}/\mathrm{d}B}{\rho_{xx}}\Big|_{B=0.} \tag{2.5}$$

2.4.3 Equipment

Room temperature Hall measurements were done with commercially available equipment that measures and gives all three values of interest: the mobility, the surface carrier density and an approximation of the volume carrier density. The method used here is called the van der Pauw method where four ohmic contacts are attached to a flat sample and resistances are measured at constant magnetic fields.

For the low temperature Hall measurements, done at a few Kelvin, a more complex measurement setup was used where the magnetic field was varied, similarly to the description in Subsection (2.4.2).

Chapter 3

XRD analysis

To be able to use the acquired data for drawing conclusions some post processing and analysis needs to be done. For the XRD scans this includes peak identification as well as some amount of error correction.

3.1 Peak identification

The lattice structure of Bi_2Te_3 is complicated, but can be analyzed as a hexagonal structure where each unit cell contains three quintuple layers of bismuth and tellurium, see Section (1.1).

The distances between two (hkl) planes in a hexagonal crystal are described by Equation (3.1):

$$\frac{1}{d^2} = \frac{4}{3}\frac{h^2 + hk + k^2}{a^2} + \frac{l^2}{c^2} \tag{3.1}$$

where d is the plane distance from Bragg's law, a and c are the two distances that define a hexagonal lattice structure and h, k and l are the plane parameters.

By scanning for $(00l)$ planes it is possible to identify the lattice constant c. The $(00l)$ planes are the only ones visible when an ω-2θ scan is done around substrate peaks since they are parallel to the surface.

3.2 Semi-automated peak search

To reliably and reproducibly find the positions of the visible peaks, a semi-automated process is needed. A rough scan and peak position identification can be done by hand,

but the peaks will in practice rarely have clear enough shapes, mainly due to noise, for this method to reliably and accurately give the peak center positions. Therefore, after manually estimating the peak positions a fit of a pseudo-Voigt profile is done using MATLAB.

A pseudo-Voigt profile is a combination of a Gauss profile and a Lorentzian profile. This is motivated by the fact that both Gaussian and Lorentzian broadening occur for the diffraction peaks for various physical reasons such as strain and size broadening. The pure Voigt profile is the convolution of the Gaussian profile and the Lorentzian profile according to Equation (3.2):

$$V(x, \sigma, \gamma) = \int_{-\infty}^{\infty} G(x', \sigma) L(x - x', \gamma) \, \mathrm{d}x' \tag{3.2}$$

where $G(x', \sigma)$ is the Gaussian profile with standard deviation σ and $L(x', \gamma)$ is the Lorentzian profile with standard deviation γ. This is however a computationally difficult profile to fit to and has thus been simplified to a pseudo-Voigt profile; the sum of a Gaussian and a Lorentzian peak[24–26]. In practice the fit also has to be around a non-zero center x_0, so the final fitting function will look like the one in Equation (3.3):

$$V_{\mathrm{p}}(x, x_0, w) = A_{\mathrm{G}} \exp\left(-4 \log(2) \frac{(x - x_0)^2}{w^2}\right) + A_{\mathrm{L}} \frac{1}{1 + 4 \frac{(x - x_0)^2}{w^2}}. \tag{3.3}$$

The fitting is done using a least-squares method with respect to the following variables: the peak center position x_0, the Gaussian amplitude A_{G}, the Lorentzian amplitude A_{L} and the full-width-half-maximum w. The reason for the presence of the seemingly arbitrary numerical constants is to make sure that the FWHM of the whole profile $V_{\mathrm{p}}(x, x_0, w)$ is w.

3.3 Sample displacement

Before the measurement, the sample is moved to a position within the X-ray beam path. Its position will however not be precise enough. Even a few micrometers of displacement in the z direction causes visible effects by displacing the peaks according to Equation (3.4)[27]:

$$\Delta\theta = -\frac{s \cos\theta}{R} \tag{3.4}$$

where R is the radius of the diffractometer and s is the displacement of the sample compared to the beam path.

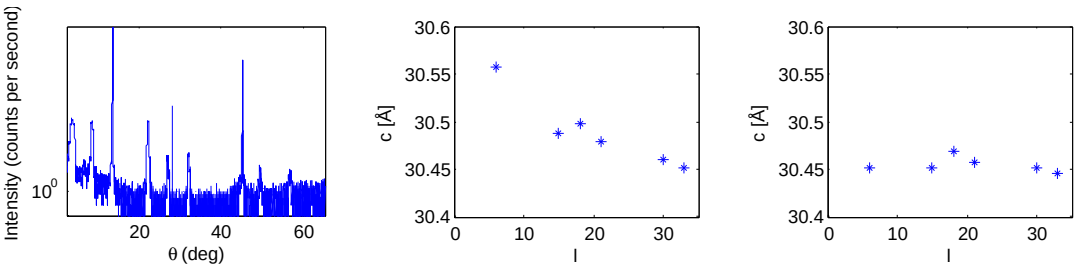

(a) Rocking curve example.

(b) Calculation of lattice constant.

(c) Calculation of lattice constant c after correcting for z axis displacement.

Figure (3.1): XRD measurement example showing the rocking curve and the resulting c lattice constant plots for each identified Bi_2Te_3 peak.

When an ω-2θ scan with multiple visible peaks is complete, it is possible to calculate and correct for this displacement by roughly identifying what planes the peaks correspond to and then minimizing the spread of the calculated lattice constants.

An example showing the effect of this can be seen in Figure (3.1). In Figure 3.1(b) the lattice constant c varies according to a decreasing pattern for each identified peak. The x axis shows the corresponding l values for the peaks. After correcting for the displacement in Figure 3.1(c) almost all peaks give the same lattice constant.

3.4 Phase identification

Since BiTe, Bi_4Te_3 and several other bismuth telluride crystals have a very similar crystal structure to Bi_2Te_3[28, 29] a method is needed to identify any samples that contain those. Bi_4Te_3 for instance, contains the same Te-Bi-Te-Bi-Te quintuple layers as Bi_2Te_3 with the difference that it has a bi-layer of bismuth between each. The unit cell is thus 42 Å tall instead of 30 Å.

A weakness in the method of peak identification shown earlier is that one has to have some vague idea about the value of the lattice constant c to be able to begin the identification. If the wrong value is chosen as starting assumption, let's say we assume $c \approx 30$ Å when in fact we have Bi_4Te_3 with $c \approx 42$Å, the peaks will be identified incorrectly.

By assuming different c values, the peaks will be identified differently. Once each peak is identified for a given assumed value of c, a real corresponding c value may be calculated using Bragg's law and Equation (3.1). The resulting values will be slightly different for each peak. If a good starting assumption was chosen for c all interesting peaks will be identified and the spread, or standard deviation, of the calculated c values will be small.

To make sure the right value is chosen, the initial c assumption can be swept over a broad range of values, including, but not limited to, the documented values for BiTe, Bi_2Te_3

and Bi_4Te_3.

The final c value that has the lowest spread among the relevant peaks will be the most likely candidate for the crystal structure.

3.5 Reciprocal space and Q scans

When plotting and analyzing mapping scans, it is often of interest to convert the coordinates to reciprocal space first. This can make it easier to relate different peaks to each other. The reciprocal coordinates are calculated using equations (3.5) and (3.6)[30]:

$$Q_x = R\left(\cos\omega - \cos\left(2\theta - \omega\right)\right), \tag{3.5}$$
$$Q_y = R\left(\sin\omega + \sin\left(2\theta - \omega\right)\right). \tag{3.6}$$

Here R is the Ewald sphere radius.

In the reciprocal space the peaks will be arranged in a rectangular grid-like manner. The $(00l)$ peaks will be along the y axis with the $(11l)$, $(\bar{1}1l)$, $(22l)$, $(\bar{2}2l)$, etc. in parallel.

3.6 Measurement accuracy

The accuracy of the XRD measurements was greatly improved by correcting for the sample displacement in the z direction. Sample displacement in x or y direction over time in the machine could however not be corrected for, neither could sample impurities.

3.6.1 Displacement over time

It is possible to combine and simplify equations (2.1) and (3.1) for $(00l)$ peaks into Equation (3.7):

$$c = \frac{\lambda l}{2\sin\theta}. \tag{3.7}$$

Using this equation it is possible to calculate a value for the lattice parameter c from every $(00l)$ diffraction peak. Observing the same diffraction peak from different angles gives a feeling regarding the uncertainty of these measurements. The (006) peak was thus measured for a sample from six different angles. The results from this measurement can be seen in Table (3.1).

The reason for the decreasing θ (and increasing c) as a function of φ can not be due to a tilt since then it would have had a sinusoidal dependence.

φ	0°	60°	120°	180°	240°	300°
θ	8.7415°	8.7387°	8.7380°	8.7379°	8.7366°	8.7356°
c	30.4112 Å	30.4209 Å	30.4233 Å	30.4237 Å	30.4282 Å	30.4316 Å

Table (3.1): Values for θ for the 006 peak from six different angles. Note that the values for c were calculated directly from the θ angles, no compensation for z displacement was possible since that would have required data from multiple peaks.

The most likely reason is that the sample had moved slightly during the long 60 hour measurement. The calibration done in the beginning with regards to the sample tilt and position was thus becoming less and less correct as time passed. Based on what is seen here, it is reasonable to expect an accuracy for c at about ± 0.01 Å.

3.6.2 Peak shifts

The main source of peak shifts is sample displacement in the z direction. After compensating for that the peaks move closer to their expected positions. Apart from the displacement, stacking faults can also cause peaks to shift by either increasing or decreasing the value of the Bragg angle θ[31, 32]. This leads to some amount of uncertainty regarding the calculated lattice parameters.

Chapter 4

Growth mode

In the ideal case, when the growth is done, there would be one single crystal of Bi_2Te_3 on the substrate. This would require either layer-by-layer growth or an island growth where the islands coalesce once they reach each other. In practice, large scale layer-by-layer growth is hard to achieve and the islands that grow do not always merge cleanly into single crystals.

The following chapter discusses how growth on different substrates in different conditions affect the sample surface and the growth mode.

4.1 Different substrates

Samples have been grown on Si(111), GaAs(100), GaAs(111) and GaN substrates. GaAs(111) substrates have two possible configurations, GaAs(111)A and GaAs(111)B. The ones that seemed most promising based on earlier measurements were the GaAs(111)B ones, so those were examined more carefully than the others. Measurements have however been done on previously grown samples as well, particularly those grown on Si(111) substrates.

4.1.1 Preparation of GaAs substrates

To compensate for any potential roughness of the substrate, an additional layer of GaAs can be grown as described in Subsection (2.1.3). The conditions during this growth are of critical importance however. If the growth conditions are chosen poorly, GaAs islands will start to grow before the surface has become smooth and the surface will end up being worse than at the start. This could potentially be due to that GaAs grows slower on the (111) plane than it does on for example the (100) plane.

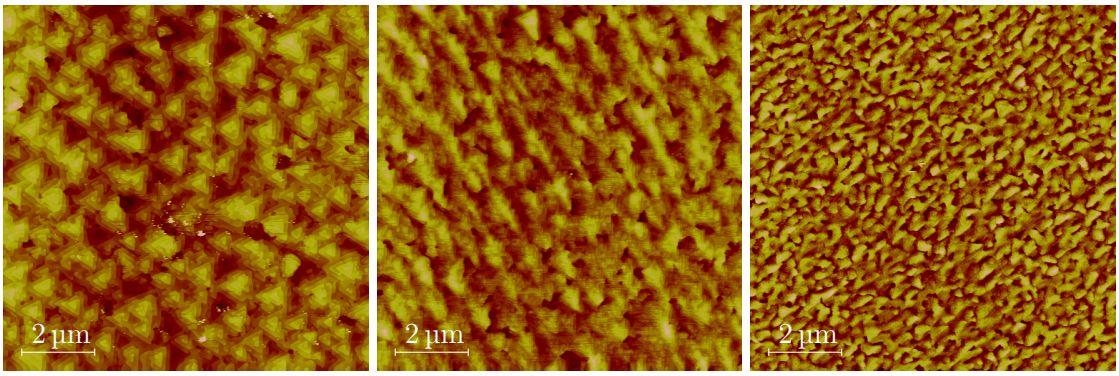

(a) Flat substrate. (b) Vicinal substrate with 1° cut. (c) Vicinal substrate with 3° cut.

Figure (4.1): 10 µm × 10 µm AFM scans of Bi_2Te_3 grown GaAs(111)B substrates with different off-cut angles.

4.1.2 Flat and vicinal substrates

The surface of the grown Bi_2Te_3 looks visibly different on vicinal GaAs(111)B substrates compared to flat ones as can be seen in Figure (4.1).

For the flat substrates we get strictly island based growth with clear triangular shaped spirals whereas for the vicinal substrates the growth mode is more complex. There is considerable island formation happening here as well, however the islands have layer-like properties. For the substrates with 1° cut the islands are not growing straight up but along the tilt of the substrate, giving a certain layer-by-layer growth look. As can be seen in Figure (4.2), there are valleys among the islands that show layer-by-layer growth. Even the islands are layered by growing in a ridge-like fashion towards one direction. For the 3° substrate the islands still have tilts, but their pointing directions are less regular.

The spiral islands on the flat substrates can grow in two possible rotation directions, clockwise and counter-clockwise. This however, does not have an effect on the island coalescence. Triangular islands pointing in the same direction with opposing spiral directions can coalesce without problems while triangles having the same spiral direction but different pointing directions have problems, see Figure (4.3) for clarification and Figure (4.4) for some examples.

4.1.3 Reproducibility

The surfaces of samples grown on substrates with a 1° vicinal angle have been quite reproducible. The direction of the tilt does not matter as can be seen in Figure (4.5). All samples have the same kind of triangular features. The tellurium flux was kept roughly the same for them as well.

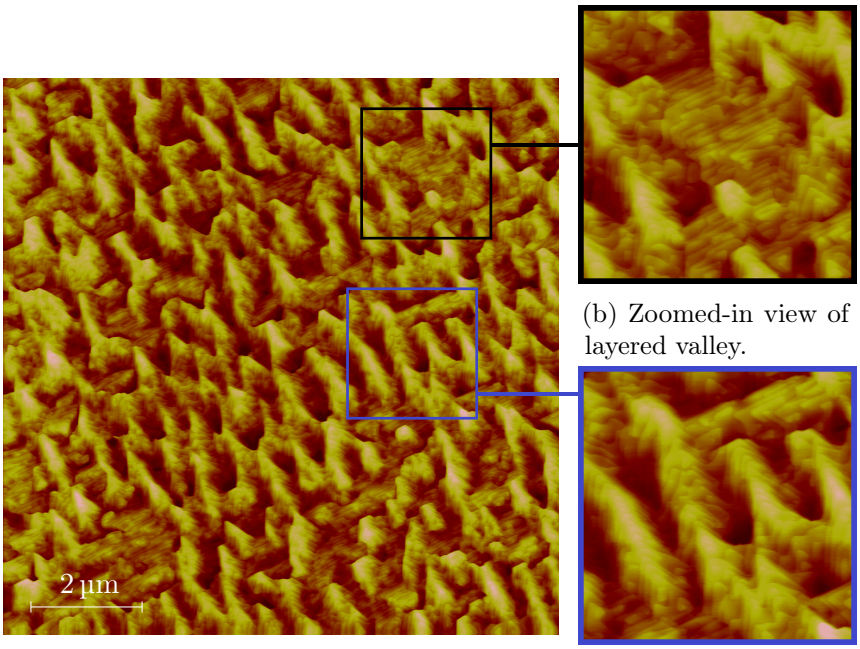

(a) 10 µm × 10 µm scan of sample R0838.

(b) Zoomed-in view of layered valley.

(c) Zoomed-in view of layered triangles causing a ridge.

Figure (4.2): AFM scan of sample on a vicinal substrate with 1° cut.

At one point, when the tellurium source in the MBE was getting depleted, the growth produced samples with the surfaces seen in Figure (4.6). Especially the sample on the vicinal substrate looked very promising. These two samples were also the only ones that showed a visible (009) peak in the XRD measurements, see Figure (4.7). Unfortunately, the continuously decreasing tellurium flux created an environment that is hard to replicate.

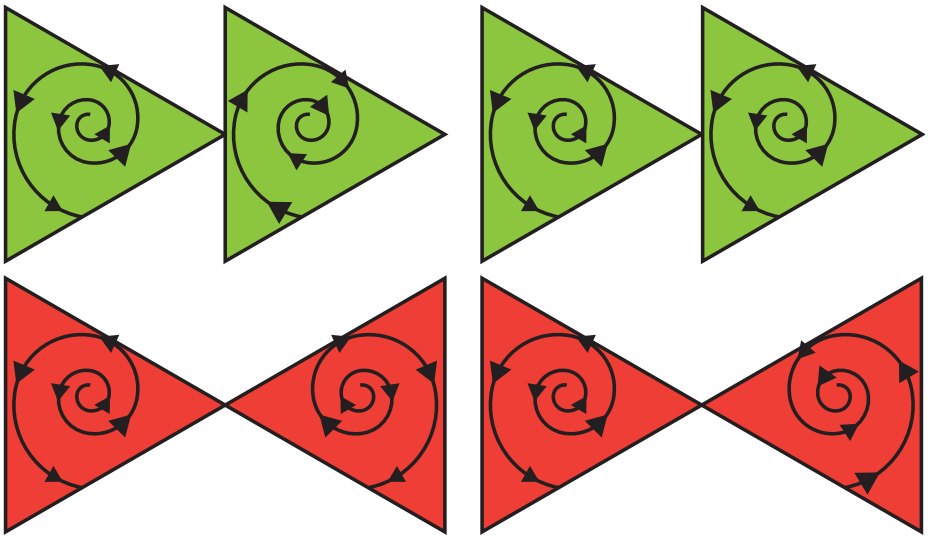

Figure (4.3): Spiral islands with the same pointing direction (upper row) coalesce irrespectively of their rotation directions while islands with different pointing directions (bottom row) do not.

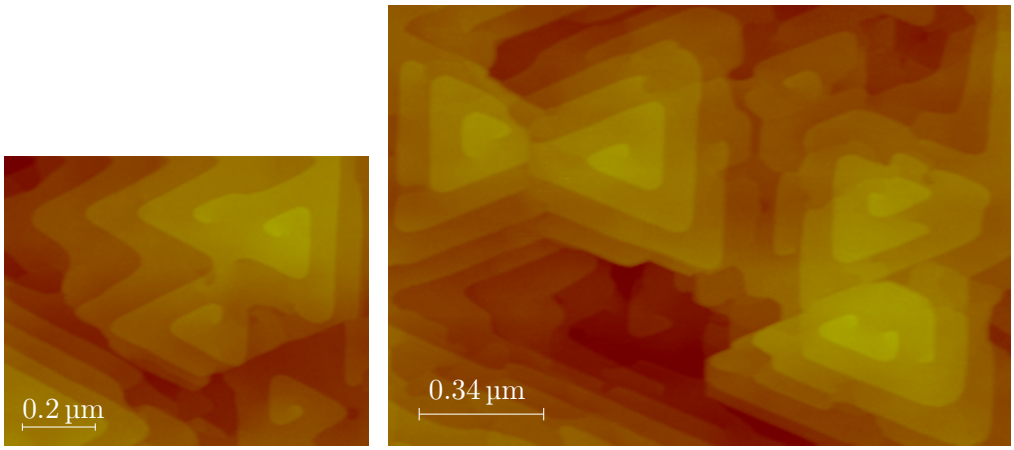

(a) One pair of coalescing spiral islands.

(b) Two pairs of non-coalescing spiral islands.

Figure (4.4): Example of meeting islands. In ((a)) the spirals have different rotational directions but the same pointing directions, while in ((b)) they have the same rotational directions but different pointing directions.

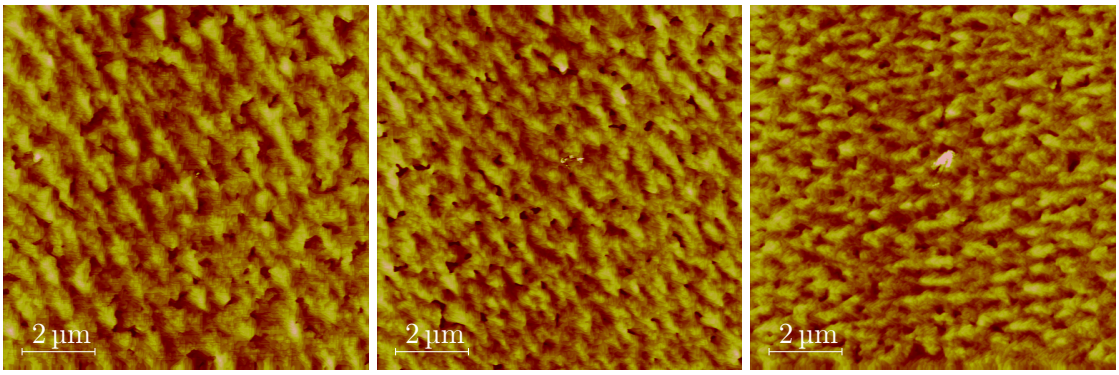

(a) 10 µm × 10 µm scan of sample R0832 with 1° tilt towards $(\bar{1}\bar{1}2)$.

(b) 10 µm × 10 µm scan of sample R0835 with 1° tilt towards $(00\bar{1})$.

(c) 10 µm × 10 µm scan of sample R0836 with 1° tilt towards (211).

Figure (4.5): AFM scans of three samples grown on vicinal GaAs(111)B substrates with 1° cuts in different directions.

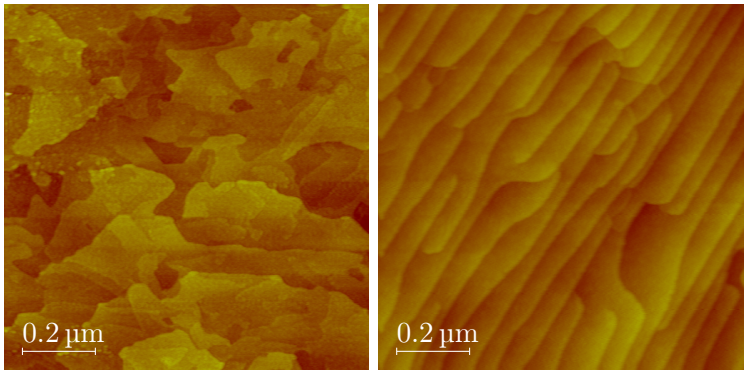

(a) 1 hour of Bi_2Te_3 growth on a flat GaAs(111)B substrate.

(b) 1 hour of Bi_2Te_3 growth on a vicinal GaAs(111)B substrate with an angle of 1°.

Figure (4.6): 1 µm × 1 µm AFM scans of samples with 1 hour of Bi_2Te_3 growth on GaAs(111)B substrates with 0° resp. 1° off-cut angles. The tellurium source was running low during the growth of these samples.

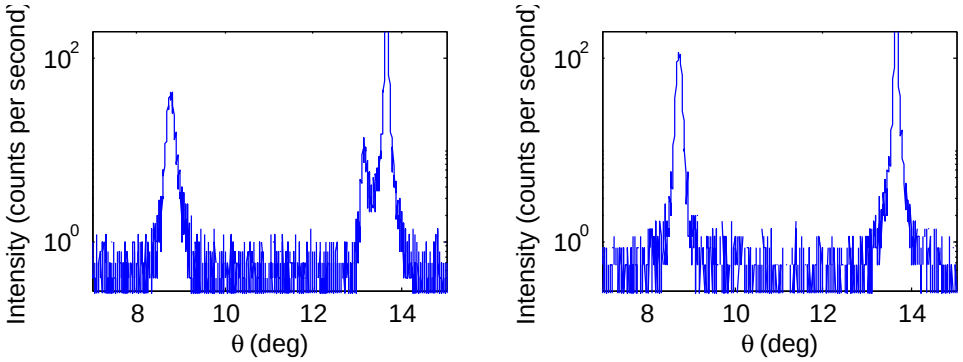

(a) Part of rocking curve for a sample with bad tellurium flux, notice the peak at $\theta = 13.14°$.

(b) Part of rocking curve for a sample with controlled tellurium flux.

Figure (4.7): Results from XRD ω-2θ scans showing the visible (009) peak for the sample with decreasing tellurium flux.

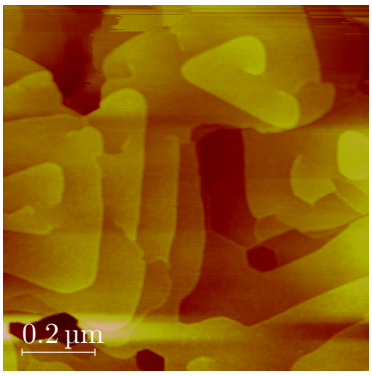

(a) 1 µm × 1 µm scan of sample R0833 with 0° angle.

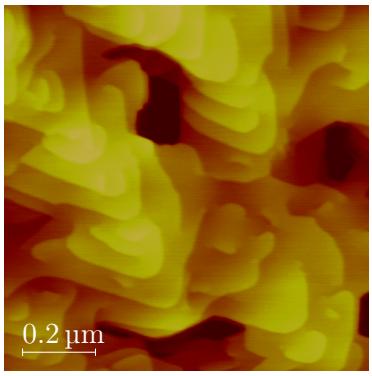

(b) 1 µm × 1 µm scan of sample R0835 with 1° angle.

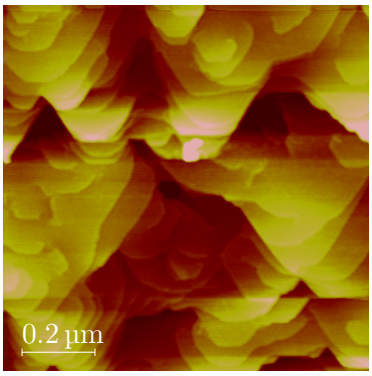

(c) 1 µm × 1 µm scan of sample R0834 with 3° angle.

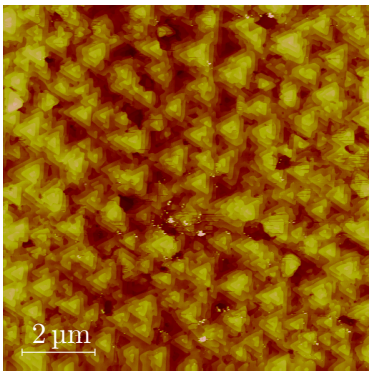

(d) 10 µm × 10 µm scan of sample R0833 with 0° angle.

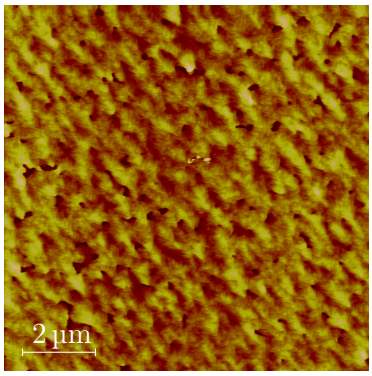

(e) 10 µm × 10 µm scan of sample R0835 with 1° angle.

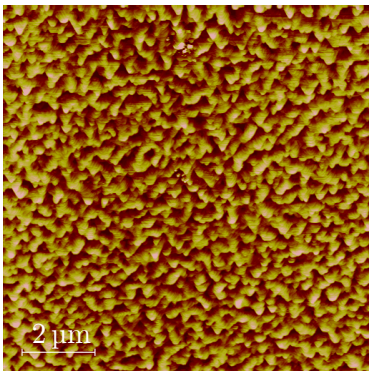

(f) 10 µm × 10 µm scan of sample R0834 with 3° angle.

Figure (4.8): AFM scans of samples grown with high tellurium flux. Te/Bi BEP was roughly 70-100.

4.2 Te/Bi BEP ratio

The Te/Bi beam equivalent pressure (BEP) ratio for the samples grown on GaAs(111)B was at first kept around 100 based on previous experiments on silicon wafers. Slightly changing the relative tellurium flux has only little effect, see figures (4.8) and (4.9). For flat substrates, lowering the tellurium flux seems to make the amount of triangles pointing in the two possible directions more even. For vicinal substrates, slightly decreasing the tellurium flux has even less visible effect.

However, lowering the Te/Bi BEP ratio too much results in an undesired change of phase. Both XRD and AFM measurements on samples grown on Si(111) substrates show that using a BEP ratio below 20 will result in Bi_4Te_3 getting deposited instead of Bi_2Te_3.

In summary, as long as the flux ratio is kept above 20-30 the growth characteristics will be quite independent of the actual ratio.

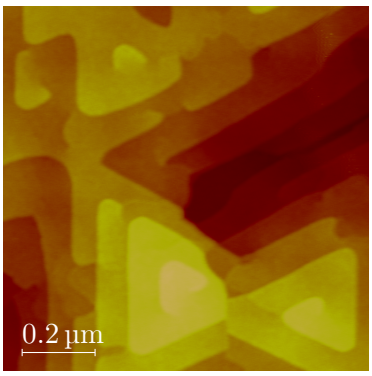

(a) 1 µm × 1 µm scan of sample R0837 with 0° angle.

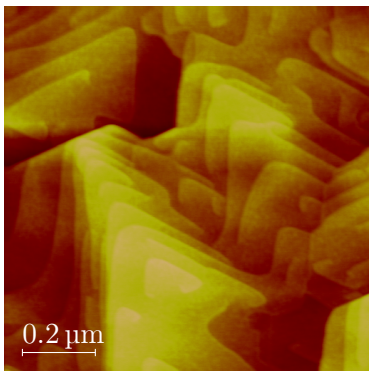

(b) 1 µm × 1 µm scan of sample R0838 with 1° angle.

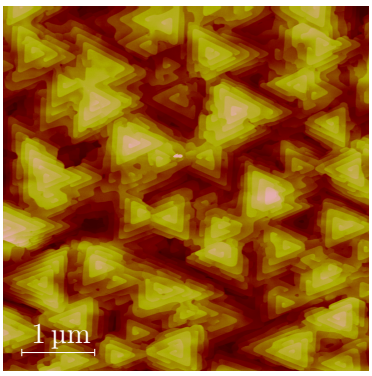

(c) 5 µm × 5 µm scan of sample R0837 with 0° angle.

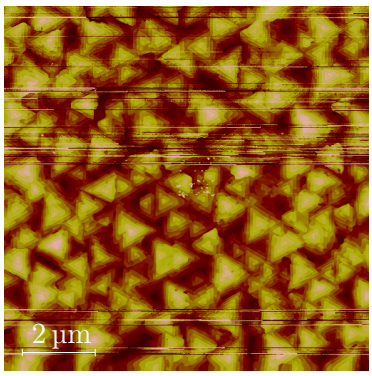

(d) 10 µm × 10 µm scan of sample R0837 with 0° angle.

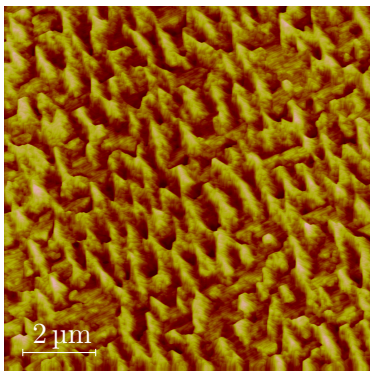

(e) 10 µm × 10 µm scan of sample R0838 with 1° angle.

Figure (4.9): AFM scans of samples grown with low tellurium flux. The Te/Bi BEP ratio was roughly 33.

Chapter 5

Phase transition

The following chapter contains results and discussions regarding the measurements showing that considerable amounts of Bi_4Te_3 gets deposited instead of Bi_2Te_3 when the tellurium flux is kept too low.

5.1 XRD scans

During MBE growth, the beam equivalent pressures (BEPs) could be adjusted for the bismuth and the tellurium sources. For samples grown on Si(111) substrates, it has been possible to see that if the relative BEP for Te/Bi gets too low, Bi_4Te_3 starts to grow instead of Bi_2Te_3.

An initial graphical indication can be seen in Figure (5.1). Note that the peaks from the Bi_4Te_3 sample almost look as if they had been shifted Bi_2Te_3 peaks with shifts in both directions.

The method used to check and identify which samples contained what is described in Section (3.4). Based on this, Table (5.1) shows a list of samples in order of Te/Bi BEP flux ratio. There is a clear correlation between the flux ratio and the composition of the deposited material.

5.2 AFM scans

To further confirm the phase transition, AFM scans were done with the intention to measure the step heights on both Bi_2Te_3 and Bi_4Te_3 samples. Since both phases consist of unit cells that can be divided into three loosely bound layers, the step heights correspond to the thickness of these. For Bi_2Te_3 this is roughly 1 nm while for Bi_4Te_3, this should be around 1.3-1.4 nm.

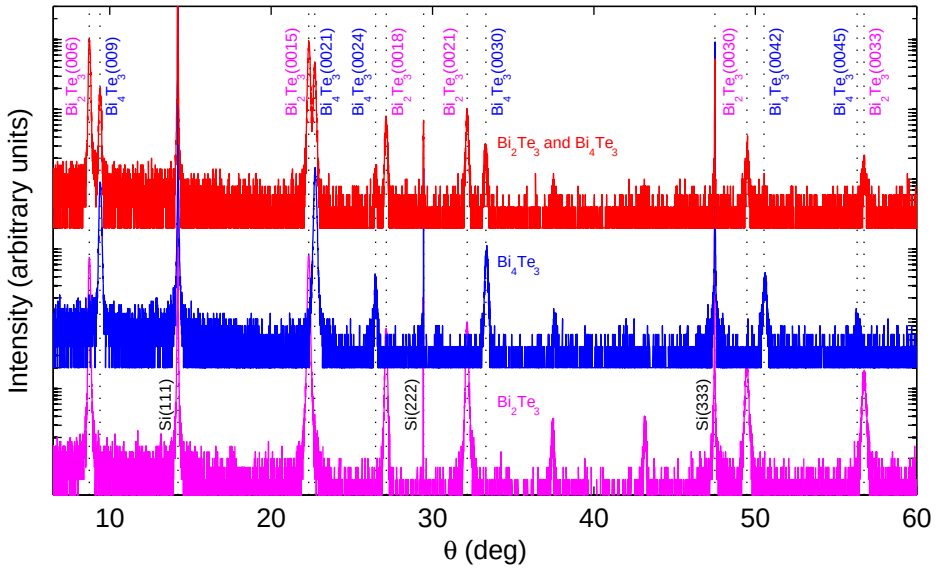

Figure (5.1): XRD ω-2θ curves of three samples. All three samples were grown on Si(111) substrates. The top two ones had 17 as Te/Bi flux ratio during growth while the bottom one had 20. Note that the top sample shows both Bi_2Te_3 and Bi_4Te_3 peaks.

Scanning several samples did indeed confirm that there is a significant difference between the two groups. AFM scans of one Bi_2Te_3 and one Bi_4Te_3 sample can be seen in Figure (5.2) together with their respective height curves. The step heights were found to be 1.00 ± 0.05 nm and 1.33 ± 0.13 nm for the Bi_2Te_3 and the Bi_4Te_3 sample respectively.

5.3 SIMS measurements

As a final way to confirm the phase transition, a selection of relevant samples were sent to DTU in Denmark where Secondary Ion Mass Spectrometry (SIMS) measurements were performed on them. SIMS measurements are performed by bombarding the sample with electrons and thus kicking the atoms out of the surface. The masses of the ejected atoms are then measured by a mass spectrometer. This can be used to analyze the composition of a sample as a function of its depth.

The results of such a measurement for two samples can be seen in Figure (5.3). It is visible that sample R0424 has 2.3 times higher Te/Bi ratio than sample R0431. This confirms the previous measurements where sample R0431 were measured to contain Bi_4Te_3, while sample R0424 contained Bi_2Te_3. Note that the absolute values of the intensities are not comparable between samples, only the relative intensities between two kinds of elements are.

Te/Bi ratio	Composition	c (Å)	Substrate	Sample id
10	Bi_4Te_3	41.67	Si(111)	R0431
17	Bi_4Te_3	41.66	Si(111)	R0664
17	Bi_2Te_3,	30.39,	Si(111)	R0661
	Bi_4Te_3	41.70		
20	Bi_2Te_3	30.42	Si(111)	R0423
20	Bi_2Te_3	30.40	Si(111)	R0424
20	Bi_2Te_3	30.40	Si(111)	R0428
20	Bi_2Te_3	30.44	Si(111)	R0671
33	Bi_2Te_3	30.47	GaAs(111)B	R0837
33	Bi_2Te_3	30.47	GaAs(111)B	R0838
75	Bi_2Te_3	30.43	GaAs(111)B	R0835
82	Bi_2Te_3	30.46	GaAs(111)B	R0836
100	Bi_2Te_3	30.47	GaAs(111)B	R0829

Table (5.1): Summary of several samples, their beam equivalent pressure ratios during growth and their compositions based on the results from the XRD measurements. Note that sample R0661 contains both Bi_2Te_3 and Bi_4Te_3.

5.4 Carrier transport

By adding extra bi-layers of bismuth to the crystal structure, in the way that Bi_4Te_3 does compared to Bi_2Te_3, the transport properties of the material change. The results shown in Figure (5.4) indicate that they do in fact become worse, at least for topological insulator applications. The carrier density is generally higher and the mobility is lower while the desired qualities are the opposite. This is most likely due to the conduction of the bismuth layers.

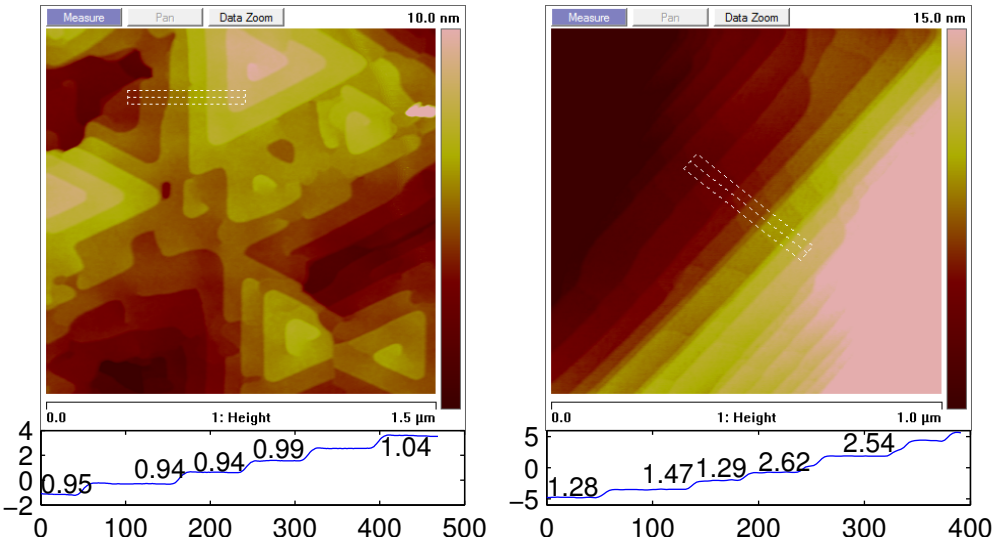

(a) AFM scan of a Bi_2Te_3 sample. (b) AFM scan of a Bi_4Te_3 sample.

Figure (5.2): Plane fitted AFM scans with marked and measured steps. Note that some of the steps are double steps.

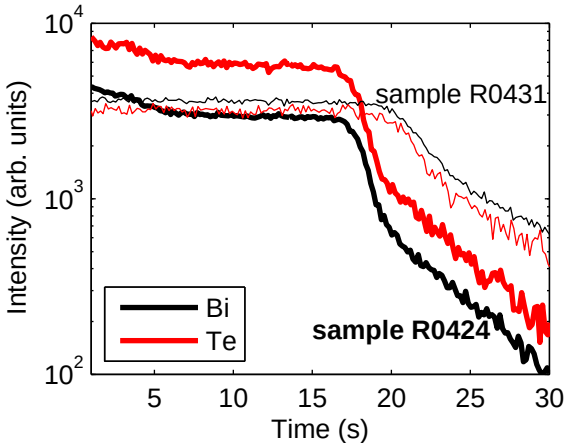

Figure (5.3): Results of two SIMS measurements. To facilitate the comparison, the data from sample R0431 has been shifted by 40 s since it was significantly thicker than sample R0424. The slight drop in the beginning of the scan for sample R0424 is a measurement artifact.

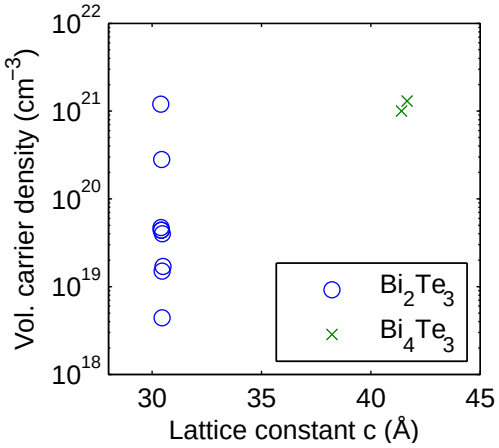

(a) Volume carrier density for the measured samples.

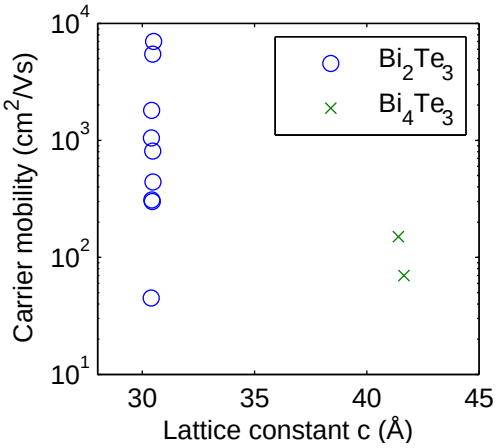

(b) Carrier mobility for the measured samples.

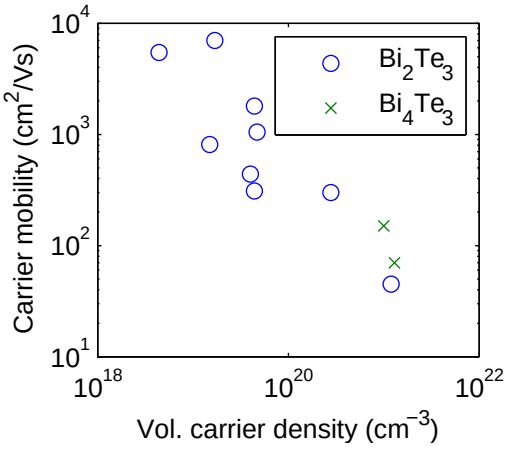

(c) Carrier mobility as a function of carrier density for the measured samples.

Figure (5.4): Results from Hall measurements done at 5 K indicating that the transport properties are worse for the Bi_4Te_3 samples than for the Bi_2Te_3 ones.

Chapter 6

Conclusions and outlook

Topological insulators in general, and bismuth telluride in particular, are interesting materials from not only a physics standpoints, but also for future applications within fields as varied as quantum computing and spintronics. The focus of this project has been to measure the quality of the growth of this material and to explore ways to improve it.

6.1 Thin film growth

The characteristics of the crystal growth depend on the conditions during growth. This affects both the crystal structure and the growth mode.

When the BEP of the tellurium source is below roughly 20 times the BEP of the bismuth source in the MBE, the deposited material is not Bi_2Te_3, but Bi_4Te_3. This has been demonstrated using XRD and verified by AFM and SIMS scans.

It has been shown that the substrate surface has considerable effect on the growth mode. When growing on vicinal GaAs(111)B substrates we have gotten clearer step-like growth along the steps of the substrate and the islands have had one clear direction. When the growth has been on flat substrates, the islands have had at least two possible orientations resulting in increased defect densities when these have met. However, on flat surfaces the islands had a clear spiral growth mode where they coalesced cleanly as long as the pointing directions of the islands were the same.

6.2 Future outlook

It will be of interest to analyze in more detail how the island growth can be affected. There are two different ways one can imagine the growth of large single crystals, either through layer-by-layer growth or by making sure that the islands coalesce without defect

formation. The smooth coalescence can be achieved by using slightly vicinal substrates, but there is still a lack of understanding about the spiral directions and their effects.

Bibliography

[1] F. J. DiSalvo, "Thermoelectric cooling and power generation," *Science*, vol. 285, no. 5428, pp. 703–706, 1999. [Online]. Available: http://dx.doi.org/10.1126/science.285.5428.703

[2] H. Zhang, C.-X. Liu, X.-L. Qi, X. Dai, Z. Fang, and S.-C. Zhang, "Topological insulators in Bi_2Se_3, Bi_2Te_3 and Sb_2Te_3 with a single Dirac cone on the surface," *Nat. Phys.*, vol. 5, pp. 438–442, Jun 2009. [Online]. Available: http://dx.doi.org/10.1038/nphys1270

[3] X. Chen, X.-C. Ma, K. He, J.-F. Jia, and Q.-K. Xue, "Molecular beam epitaxial growth of topological insulators," *Adv. Mater.*, vol. 23, no. 9, pp. 1162–1165, 2011. [Online]. Available: http://dx.doi.org/10.1002/adma.201003855

[4] H. Liu, H. Yuan, N. Fukui, L. Zhang, J. Jia, Y. Iwasa, M. Chen, T. Hashizume, T. Sakurai, and Q. Xue, "Growth of topological insulator bi2te3 ultrathin films on si(111) investigated by low-energy electron microscopy," *Cryst. Growth Des.*, vol. 10, no. 10, pp. 4491–4493, 2010. [Online]. Available: http://dx.doi.org/10.1021/cg1007457

[5] O. Madelung, U. Rössler, and M. Schulz, Eds., ser. Landolt-Börnstein - Group III Condensed Matter. Springer-Verlag, 1998, vol. 41C, ch. Bismuth telluride (Bi2Te3) crystal structure, chemical bond, lattice parameters (including data for related compounds). [Online]. Available: http://dx.doi.org/10.1007/10681727_976

[6] J. E. Moore and L. Balents, "Topological invariants of time-reversal-invariant band structures," *Phys. Rev. B*, vol. 75, no. 12, p. 121306, Mar 2007. [Online]. Available: http://dx.doi.org/10.1103/PhysRevB.75.121306

[7] M. Z. Hasan and C. L. Kane, "Colloquium: Topological insulators," *Rev. Mod. Phys.*, vol. 82, pp. 3045–3067, Nov 2010. [Online]. Available: http://dx.doi.org/10.1103/RevModPhys.82.3045

[8] K. v. Klitzing, G. Dorda, and M. Pepper, "New method for high-accuracy determination of the fine-structure constant based on quantized hall resistance," *Phys. Rev. Lett.*, vol. 45, pp. 494–497, Aug 1980. [Online]. Available: http://dx.doi.org/10.1103/PhysRevLett.45.494

[9] R. E. Prange and S. M. Girvin, in *The Quantum Hall Effect*. Springer US, 1987. [Online]. Available: http://dx.doi.org/10.1007/978-1-4684-0499-9

[10] C. L. Kane and J. E. Moore, "Topological insulators," *Phys. World*, vol. 24, pp. 32–36, Feb 2011.

[11] J. E. Moore, "The birth of topological insulators," *Nature*, vol. 464, no. 7286, pp. 194–198, Mar 2010. [Online]. Available: http://dx.doi.org/10.1038/nature08916

[12] H. C. Manoharan, "Topological insulators: A romance with many dimensions," *Nat. Nanotechnol.*, vol. 5, no. 7, pp. 477–479, Jul 2010. [Online]. Available: http://dx.doi.org/10.1038/nnano.2010.138

[13] A. Cho and J. Arthur, "Molecular beam epitaxy," *Progress in Solid State Chemistry*, vol. 10, Part 3, pp. 157 – 191, 1975. [Online]. Available: http://dx.doi.org/10.1016/0079-6786(75)90005-9

[14] Y.-Y. Li, G. Wang, X.-G. Zhu, M.-H. Liu, C. Ye, X. Chen, Y.-Y. Wang, K. He, L.-L. Wang, X.-C. Ma, H.-J. Zhang, X. Dai, Z. Fang, X.-C. Xie, Y. Liu, X.-L. Qi, J.-F. Jia, S.-C. Zhang, and Q.-K. Xue, "Intrinsic topological insulator Bi_2Te_3 thin films on Si and their thickness limit," *Adv. Mater.*, vol. 22, no. 36, pp. 4002–4007, 2010. [Online]. Available: http://dx.doi.org/10.1002/adma.201000368

[15] H. D. Li, Z. Y. Wang, X. Kan, X. Guo, H. T. He, Z. Wang, J. N. Wang, T. L. Wong, N. Wang, and M. H. Xie, "The van der Waals epitaxy of Bi_2Se_3 on the vicinal Si(111) surface: an approach for preparing high-quality thin films of a topological insulator," *New Journal of Physics*, vol. 12, no. 10, p. 103038, 2010. [Online]. Available: http://dx.doi.org/10.1088/1367-2630/12/10/103038

[16] Z. Y. Wang, H. D. Li, X. Guo, W. K. Ho, and M. H. Xie, "Growth characteristics of topological insulator Bi_2Se_3 films on different substrates," *Journal of Crystal Growth*, vol. 334, no. 1, pp. 96 – 102, 2011. [Online]. Available: http://dx.doi.org/10.1016/j.jcrysgro.2011.08.029

[17] M. H. Xie, L. X. Zheng, S. H. Cheung, Y. F. Ng, H. Wu, S. Y. Tong, and N. Ohtani, "Reduction of threading defects in GaN grown on vicinal SiC(0001) by molecular-beam epitaxy," *Applied Physics Letters*, vol. 77, no. 8, pp. 1105 –1107, aug 2000. [Online]. Available: http://dx.doi.org/10.1063/1.1289266

[18] X. R. Huang, J. Bai, M. Dudley, B. Wagner, R. F. Davis, and Y. Zhu, "Step-controlled strain relaxation in the vicinal surface epitaxy of nitrides," *Phys. Rev. Lett.*, vol. 95, p. 086101, Aug 2005. [Online]. Available: http://dx.doi.org/10.1103/PhysRevLett.95.086101

[19] Z. Zeng, T. A. Morgan, D. Fan, C. Li, Y. Hirono, X. Hu, J. S. Lee, Z. M. Wang, J. Wang, S. Yu, M. E. Hawkridge, M. Benamara, and G. J. Salamo, "Molecular beam epitaxial growth of Bi_2Te_3 and Sb_2Te_3 topological insulators on GaAs (111)

substrates: A potential route to fabricate topological insulator p-n junction," *ArXiv e-prints*, Jan. 2013. [Online]. Available: http://arxiv.org/abs/1301.0362

[20] Furiouslettuce, "Bragg diffraction planes," Apr. 2009. [Online]. Available: http://commons.wikimedia.org/wiki/File:BraggPlaneDiffraction.svg

[21] U. Vainio, "X-ray diffraction transmission," Nov. 2006. [Online]. Available: http://commons.wikimedia.org/wiki/File:X-ray_diffraction_transmission.svg

[22] OverlordQ, "Atomic force microscope block diagram," Oct. 2009. [Online]. Available: http://commons.wikimedia.org/wiki/File:Atomic_force_microscope_block_diagram.svg

[23] T. Ihn, "Diffusive classical transport in two-dimensional electron gases," in *Semiconductor Nanostructures: Quantum states and electronic transport*. Oxford University Press Inc., 2009, ch. 10, pp. 143–174.

[24] E. Whiting, "An empirical approximation to the Voigt profile," *Journal of Quantitative Spectroscopy and Radiative Transfer*, vol. 8, no. 6, pp. 1379 – 1384, 1968. [Online]. Available: http://dx.doi.org/10.1016/0022-4073(68)90081-2

[25] G. K. Wertheim, M. A. Butler, K. W. West, and D. N. E. Buchanan, "Determination of the Gaussian and Lorentzian content of experimental line shapes," *Review of Scientific Instruments*, vol. 45, no. 11, pp. 1369–1371, 1974. [Online]. Available: http://dx.doi.org/10.1063/1.1686503

[26] F. Sánchez-Bajo and F. L. Cumbrera, "The use of the pseudo-Voigt function in the variance method of X-ray line-broadening analysis," *Journal of Applied Crystallography*, vol. 30, no. 4, pp. 427–430, Aug 1997. [Online]. Available: http://dx.doi.org/10.1107/S0021889896015464

[27] G. Riva, M. Vanelli, and G. Airoldi, "A new calibration method for the x-ray powder diffraction study of shape memory alloys," *Phys. Status Solidi A*, vol. 148, no. 2, pp. 363–372, 1995. [Online]. Available: http://dx.doi.org/10.1002/pssa.2211480204

[28] K. Yamana, K. Kihara, and T. Matsumoto, "Bismuth tellurides: BiTe and Bi_4Te_3," *Acta Cryst. B*, vol. 35, no. 1, pp. 147–149, Jan 1979. [Online]. Available: http://dx.doi.org/10.1107/S0567740879002788

[29] J. W. G. Bos, H. W. Zandbergen, M.-H. Lee, N. P. Ong, and R. J. Cava, "Structures and thermoelectric properties of the infinitely adaptive series $(Bi_2)_m(Bi_2Te_3)_n$," *Phys. Rev. B*, vol. 75, p. 195203, May 2007. [Online]. Available: http://link.aps.org/doi/10.1103/PhysRevB.75.195203

[30] PANalytical, *X'Pert Epitaxy manual*, Jan 2004, X'Pert Epitaxy ver. 4.1.

[31] J. Makinson, J. Lee, S. Magner, R. De Angelis, W. Weins, and A. Hieronymus, "X-ray diffraction signatures of defects in nanocrystalline materials," *Advances in X-ray Analysis*, vol. 42, 2000.

[32] B. E. Warren, "Diffraction by imperfect crystals," in *X-Ray Diffraction*. Dover Publications Inc., 1969, ch. 13, pp. 251–314.